



Fine Control of Perovskite Crystallization and Reducing Luminescence Quenching Using Self-Doped Polyaniline Hole Injection Layer for Efficient Perovskite Light-Emitting Diodes

Soyeong Ahn, Min-Ho Park, Su-Hun Jeong, Young-Hoon Kim, Jinwoo Park, Sungjin Kim, Hobeom Kim, Himchan Cho, Christoph Wolf, Mingyuan Pei, Hoichang Yang, and Tae-Woo Lee*

Organic–inorganic hybrid perovskites (OHPs) are promising emitters for light-emitting diodes (LEDs) due to the high color purity, low cost, and simple synthesis. However, the electroluminescent efficiency of polycrystalline OHP LEDs (PeLEDs) is often limited by poor surface morphology, small exciton binding energy, and long exciton diffusion length of large-grain OHP films caused by uncontrolled crystallization. Here, crystallization of methylammonium lead bromide (MAPbBr₃) is finely controlled by using a polar solvent-soluble self-doped conducting polymer, poly(styrenesulfonate)-grafted polyaniline (PSS-g-PANI), as a hole injection layer (HIL) to induce granular structure, which makes charge carriers spatially confined more effectively than columnar structure induced by the conventional poly(3,4-ethylenedioxythiophene):polystyrenesulfonate (PEDOT:PSS). Moreover, lower acidity of PSS-g-PANI than PEDOT:PSS reduces indium tin oxide (ITO) etching, which releases metallic In species that cause exciton quenching. Finally, doubled device efficiency of 14.3 cd A⁻¹ is achieved for PSS-g-PANI-based polycrystalline MAPbBr₃ PeLEDs compared to that for PEDOT:PSS-based PeLEDs (7.07 cd A⁻¹). Furthermore, PSS-g-PANI demonstrates high efficiency of 37.6 cd A⁻¹ in formamidinium lead bromide nanoparticle LEDs. The results provide an avenue to both control the crystallization kinetics and reduce the migration of In released from ITO by forming OIP films favorable for more radiative luminescence using the polar solvent-soluble and low-acidity polymeric HIL.

1. Introduction

Organic–inorganic hybrid perovskite (OHP) exhibits electroluminescence (EL) with high color purity (full width at half maximum [FWHM] ≈20 nm) and their emission color is easily tuned. Also, they are solution-processable and inexpensive so they show promise as emitting materials for light-emitting diodes (LEDs).^[1–9] However, conventional solution-processing methods such as spin-coating, inkjet-printing, and bar-coating processes to deposit polycrystalline OHP films yield incomplete surface coverage or poor surface morphology, which induces leakage current caused by pores between grains and nonradiative recombination caused by defects in grain boundaries, and thus these degrade the device efficiency of OHP LEDs (PeLEDs).^[3,5,10,11] Furthermore, these conventional solution processes without additional post-processing such as nanocrystal pinning (NCP) process yield large grains, which cause long exciton diffusion length and the small exciton binding energy of the polycrystalline OHP films.^[3,6,12,13]

S. Ahn
Department of Materials Science and Engineering
Pohang University of Science and Technology (POSTECH)
77 Cheongam-Ro, Nam-Gu, Pohang, Gyeongbuk 37673, Republic of Korea
Dr. M.-H. Park, Dr. S.-H. Jeong, Dr. Y.-H. Kim, Dr. H. Kim,
Dr. H. Cho, Dr. C. Wolf
Research Institute of Advanced Materials
Seoul National University
1 Gwanak-ro, Gwanak-gu, Seoul 08826, Republic of Korea
J. Park, S. Kim
Department of Materials Science and Engineering
Seoul National University
1 Gwanak-ro, Gwanak-gu, Seoul 08826, Republic of Korea

M. Pei, Prof. H. Yang
Department of Chemical Engineering
Inha University
100 Inha-ro, Michuhol-gu, Incheon 22212, Republic of Korea
Prof. T.-W. Lee
Department of Materials Science and Engineering
Institute of Engineering Research
Research Institute of Advanced Materials
Nano Systems Institute (NSI)
BK21 PLUS SNU Materials Division for Educating
Creative Global Leaders
Seoul National University
1 Gwanak-ro, Gwanak-gu, Seoul 08826, Republic of Korea
E-mail: twlees@snu.ac.kr

The ORCID identification number(s) for the author(s) of this article can be found under <https://doi.org/10.1002/adfm.201807535>.

DOI: 10.1002/adfm.201807535

Reducing the grain size to spatially confine the excitons inside small grains can effectively increase radiative recombination rate and thus device efficiency can be improved.^[3,6,11,14,15] NCP process is one of the effective methods to form small grains through the volatile-nonpolar-solvent-induced rapid crystallization that can induce notably smooth and uniform surface morphology with small nanograins in polycrystalline OHP films while avoiding rough and nonuniform surface morphology with many large cuboids. The improved surface morphology with small grains contributed to significantly increasing the external quantum efficiency (EQE) of polycrystalline methylammonium lead bromide (MAPbBr₃) PeLEDs to 8.79%.^[3,7] Recently, high EQEs of PeLEDs (10.4% for methylammonium lead iodide (MAPbI₃) and 9.3% for MAPbBr₃) have been achieved by adding long chain ammonium halide such as butylammonium iodide or butylammonium bromide, which impeded the grain growth and thereby dramatically reduced the grain size (≈ 10 nm), to the perovskite precursors.^[6] These improvements in the device efficiencies of polycrystalline PeLEDs resulting from enhanced exciton confinement imply the need for the promising approach to reduce the grain size of OHPs.^[6]

Reducing the exciton quenching at the interfaces between adjacent layers is also imperative to improve EL efficiency of PeLEDs. During the device fabrication process, the surface of indium tin oxide (ITO) anode is severely etched by the highly acidic poly(3,4-ethylenedioxy thiophene):poly(styrene sulfonic acid) (PEDOT:PSS), which is the most widely used polymeric hole injection layer (HIL) in solution-processed PeLEDs, is spin-coated onto ITO, and thus it causes the exciton quenching at the HIL/OHP layer by the migration of metallic species such as Indium (In) close to the recombination zone in the emitting OHP layer.^[16–18] To avoid the exciton quenching caused by diffused metallic In species released from etched ITO, other anode materials such as graphene or fluorinated conducting polymer have been suggested for PeLEDs.^[3,19] The chemically inert graphene anode induced higher PL intensity, longer PL lifetime, and higher EL efficiency in polycrystalline OHP films and PeLEDs than the counterparts using the ITO anode. It supports the influence of In diffusion on the exciton quenching in PeLEDs using ITO.^[19] Therefore, it is quite imperative to develop less-acidic conducting polymer HIL instead of using highly acidic PEDOT:PSS HIL on ITO to minimize the exciton quenching caused by metallic In migration.

Here, we incorporated a self-doped conducting polymer, poly(styrenesulfonate)-g-polyaniline (PSS-g-PANI), as the HIL in polycrystalline PeLEDs to make smooth and granular nanograin OHP structure and reduce the exciton quenching by diffused metallic In species released from etched ITO electrode. We noticed that: i) a polar solvent-soluble conducting polymer can effectively delay the evaporation of the good solvent (i.e., dimethyl sulfoxide [DMSO]) for dissolving OHP precursors during the MAPbBr₃ formation. The delayed evaporation of good solvent facilitates the control of the OHP morphology when the additive-based nanocrystal pinning (A-NCP) method is adopted to reduce the grain size.^[3,7] We also noticed that ii) low acidity of an overlying conducting polymer can suppress chemical etching on the ITO, and thus it can effec-

tively reduce the exciton quenching caused by the diffused metallic species etched from the ITO. Therefore, PSS-g-PANI, a polar solvent-soluble and low-acidic polymeric HIL, effectively improved the OHP film morphology during the film-forming process combined with the A-NCP method. We achieved a uniform and pinhole-free MAPbBr₃ film with closely packed small grains and the granular crystal structure which leads to more effective exciton confinement and radiative recombination than the pristine MAPbBr₃ film with the columnar crystal structure. As a consequence of these superior effects of PSS-g-PANI to PEDOT:PSS, the device efficiency was approximately doubled from 7.07 cd A⁻¹ in PEDOT:PSS-based PeLEDs to 14.3 cd A⁻¹ in PSS-g-PANI-based PeLEDs. Moreover, formamidinium lead bromide (FAPbBr₃) nanoparticle (NP) LEDs using PSS-g-PANI as a HIL achieved significantly high current efficiency (CE) of 37.6 cd A⁻¹.

2. Results and Discussion

The chemical structures of PEDOT:PSS and PSS-g-PANI are presented in **Figure 1a,b**. To investigate the film characteristics of the conducting polymers, the root-mean-square surface roughness R_{rms} and wetting property of PEDOT:PSS and PSS-g-PANI films were analyzed by atomic force microscopy (AFM) and contact angle measurement, respectively (Figures S1 and S2, Supporting Information). As a result of the use of the PSS template in the conducting polymer solution, both PEDOT:PSS and PSS-g-PANI films showed high uniformity and smooth surfaces; PSS-g-PANI had $R_{\text{rms}} = 0.514$ nm and PEDOT:PSS had $R_{\text{rms}} = 0.932$ nm. In PSS-g-PANI, PSS template binds covalently to the polyaniline (PANI), so PSS-g-PANI showed exceptional film-forming property and the film surfaces were completely wetted by polar solvents such as water and DMSO (Figure S2a,b, Supporting Information). The DMSO is generally chosen as a solvent for dissolving perovskite precursors, including MAPbBr₃ precursors so the solubility of PSS-g-PANI in DMSO heavily influences the crystallization of the MAPbBr₃ as confirmed by a change in the film's color.^[20] Crystallization of MAPbBr₃ took >50 s longer on PSS-g-PANI than on PEDOT:PSS (Figure 1c,d). The original crystallization time t_{CO} was defined as the time when the film's color changed from transparent to opaque greenish orange: the t_{CO} of MAPbBr₃ was ≈ 120 s on PEDOT:PSS and ≈ 170 s on PSS-g-PANI.

Generally, the surface properties of HIL affect the crystallization. However, the surface compositions of PEDOT:PSS and PSS-g-PANI do not show much difference because both include a significantly large amount of PSS (Figure S3, Supporting Information). We ascribed the delayed crystallization time on the PSS-g-PANI film to the slow evaporation of DMSO caused by the solubility of PSS-g-PANI in DMSO. PEDOT:PSS also has the polar solvent-soluble PSS template which can make insoluble PEDOT dispersed in aqueous solution but, in PEDOT:PSS, PEDOT is just ionically bonded to PSS while PANI is covalently bonded to PSS in PSS-g-PANI. So, the solubility of PEDOT:PSS films in a polar solvent DMSO is much lower than that of PSS-g-PANI films.

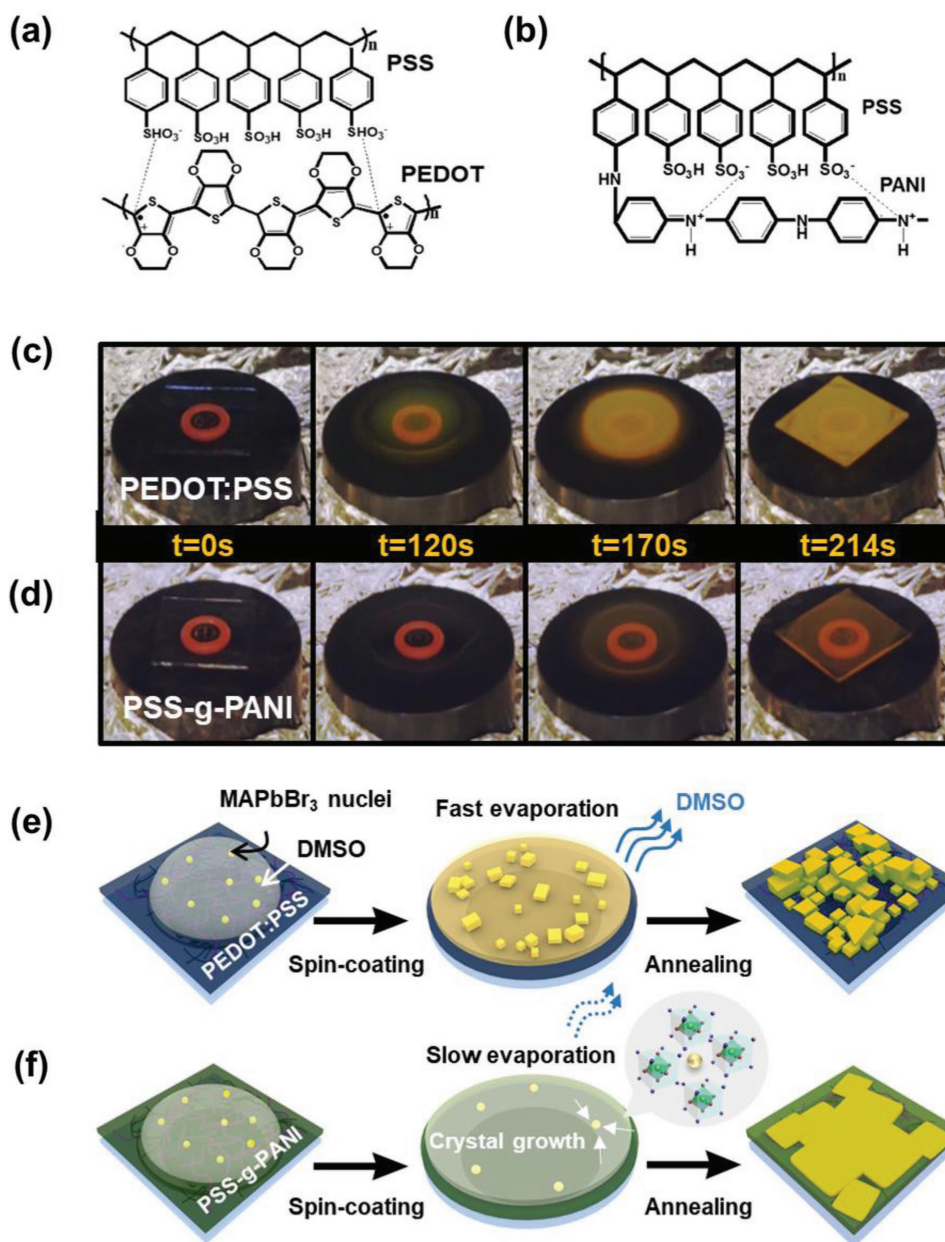


Figure 1. Chemical structures of a) PEDOT:PSS and b) PSS-g-PANI. Real-time pictures and schematic images of crystallization of MAPbBr₃ on c,e) PEDOT:PSS and d,f) PSS-g-PANI during the spin-coating process over time.

To clarify how the solubility of the under layer in the polar solvent affected the crystallization time of the overlying MAPbBr₃, we compared the crystallization times of MAPbBr₃ on PEDOT:PSS, PSS-g-PANI, and PSS (Movie S1, Supporting Information). The time required for crystallization increased with an increase in the solubility of the under layer in the polar solvent (PEDOT:PSS < PSS-g-PANI < PSS). When MAPbBr₃/DMSO precursor solution is loaded on the PSS-g-PANI film, the strong attraction between PSS-g-PANI and DMSO causes the solution to spread and soak into the film immediately (Figure S2, Supporting Information); these responses impede the evaporation of DMSO from the spinning

substrate. This slow evaporation can lead to the formation of large perovskite crystals (Figure 1e,f). MAPbBr₃ grains were almost ten times larger on PSS-g-PANI (≈20 μm) than on PEDOT:PSS (≈2 μm) (Figure 2a,b); this difference is consistent with our hypothesis that the DMSO evaporates more slowly on PSS-g-PANI.^[21]

We also investigated the crystal structures of the perovskite layer formed on PEDOT:PSS and PSS-g-PANI by measuring X-ray diffraction (XRD) (Figure 2c,d). The XRD peaks of MAPbBr₃ on PEDOT:PSS were assigned to (100), (110), (200), (210), (211), (220), and (300) crystal planes which are identical to the previously reported results.^[3,7] The XRD patterns

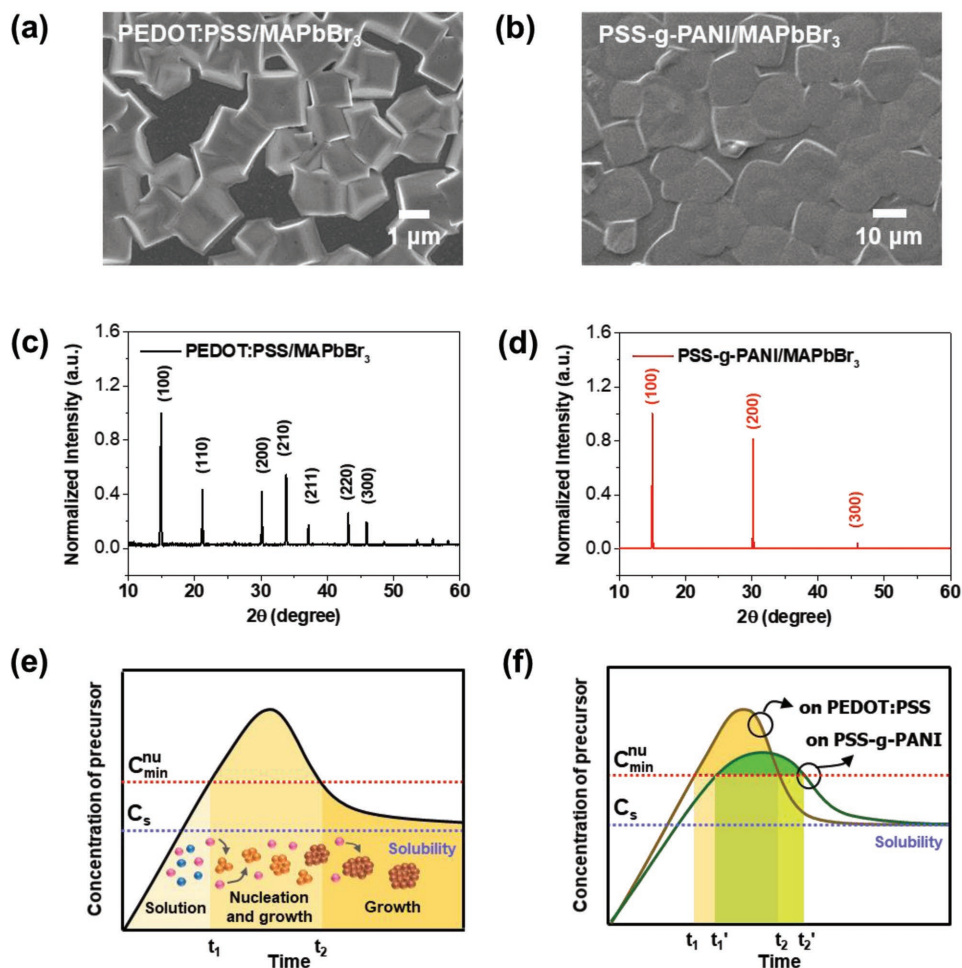


Figure 2. SEM images and XRD spectra of MAPbBr₃ formed via normal spin-coating process on a,c) PEDOT:PSS and b,d) PSS-g-PANI. e) LaMer diagram and f) modified LaMer diagram for MAPbBr₃ formation on PEDOT:PSS and on PSS-g-PANI.

of the MAPbBr₃ on PSS-g-PANI showed only three main peaks which correspond to (100), (200), and (300), respectively. 2D grazing-incidence X-ray diffraction (GIXD) patterns of MAPbBr₃ on PSS-g-PANI demonstrate that the perovskite has preferred orientation (Figure S4, Supporting Information). These results proved that the MAPbBr₃ crystals grow laterally on PSS-g-PANI, as it can be expected from the scanning electron microscope (SEM) image.^[22] DMSO has high surface tension so the MAPbBr₃ can grow laterally during the spin-coating process; therefore, the huge difference in the shape of the MAPbBr₃ crystals may be a consequence of the difference in the amount of remaining DMSO on PEDOT:PSS and on PSS-g-PANI.^[22]

The morphology of the MAPbBr₃ film is highly affected by the crystallization kinetics, which is closely related to the solvent evaporation rate. LaMer's nucleation theory suggests that the nucleation and growth processes are dependent on the time trend in solution concentration (Figure 2e).^[23] As the solvent continuously evaporates, it reaches supersaturation concentration C_s . However, the nucleation only occurs after the energy barrier for nucleation is overcome, so nucleation begins when the concentration exceeds the minimum concentration $C_{nu,min}$.

Then, the nuclei grow by consuming the solute in the precursor solution.^[21] When the solvent evaporates slowly, this growth process can take place rapidly so that solute is consumed quickly. When the solvent evaporates quickly, the solution concentration is likely to be in the region above $C_{nu,min}$ (nucleation period), so nucleation and growth are vigorous.^[21] This theory suggests that the bigger grain size of MAPbBr₃ on PSS-g-PANI than on PEDOT:PSS is due to slower solvent evaporation on PSS-g-PANI than on PEDOT:PSS.

We suggested the crystallization processes of MAPbBr₃ on PEDOT:PSS and on PSS-g-PANI hypothetically, based on LaMer's theory and our results (Figure 2f). On PEDOT:PSS, the DMSO evaporates rapidly, so MAPbBr₃ crystals have gone through fast nucleation and growth processes as soon as the precursor concentration reaches $C_{nu,min}$. On PSS-g-PANI, the DMSO evaporates slowly, so the time for the precursor concentration to reach C_s is longer than in the PEDOT:PSS/MAPbBr₃ system. As soon as the nucleation occurs, the nuclei grow fast by consuming the solute in the precursor. Therefore, in the nucleation period (t_1-t_2 for PEDOT:PSS/MAPbBr₃, $t'_1-t'_2$ for PSS-g-PANI/MAPbBr₃), the precursor concentration on PSS-g-PANI is lower than on PEDOT:PSS. However, considering the large

crystal size distribution on PSS-g-PANI, the nucleation period of PSS-g-PANI/MAPbBr₃ is expected to be longer than that of PEDOT:PSS/MAPbBr₃. It is supported by the SEM image in Figure 2b. The growth of MAPbBr₃ on PSS-g-PANI continues even when the crystallization of MAPbBr₃ on PEDOT:PSS is over because DMSO remains on the PSS-g-PANI film.

To achieve high EL efficiency in PeLEDs, the grain size of the MAPbBr₃ should be small, so we used the A-NCP to form uniform nanograin OHP films.^[3,7] The NCP induces solvent-mediated fast crystallization to stop the grain growth and thereby to confine the excitons spatially. A volatile nonpolar solvent, chloroform (CF), is introduced to remove the DMSO from the MAPbBr₃/DMSO film. The A-NCP solution includes 2,2',2''-(1,3,5-benzotriptyl)-tris(1-phenyl-1-H-benzimidazole) (TPBi) as an electron-transporting additive that heals defects.^[7] The slow rate of solvent evaporation on PSS-g-PANI gives enough time for the nonpolar solvent dripping, so the use of PSS-g-PANI as an interfacial layer was more beneficial than PEDOT:PSS to control the perovskite morphology when the A-NCP was used (Figure 3a,b). We obtained highly uniform MAPbBr₃ films with reduced grain size on both PEDOT:PSS and PSS-g-PANI (Figure 3) and their crystal structures were identical (Figures S4 and S5, Supporting Information), but the grain sizes were smaller and their size distribution was narrower on PSS-g-PANI than on PEDOT:PSS (Figure S6, Supporting Information).

The A-NCP accelerates crystal nucleation and growth and terminates the crystallization by causing fast supersaturation, so the t_{C0} and the time point at which A-NCP is conducted are decisive factors that determine the morphology of the MAPbBr₃ film. Since t_{C0} of MAPbBr₃ was longer on PSS-g-PANI (≈ 170 s) than on PEDOT:PSS (≈ 120 s) (Figure 1c,d), the time range of A-NCP for MAPbBr₃ on PSS-g-PANI is wider than on PEDOT:PSS. We controlled the A-NCP time point (Figure 3a,b) (at -50 and -20 s before t_{C0} for MAPbBr₃ on PEDOT:PSS, and -60 , -50 , -40 , and -20 s before t_{C0} for MAPbBr₃ on PSS-g-PANI) and investigated the morphologies of the resultant films by capturing top-view and cross-sectional SEM images (Figure 3c–h).

The grain size decreased as A-NCP is conducted earlier. This trend indicates that the growth of the MAPbBr₃ was ongoing continuously. Also, the structure of the MAPbBr₃ films on PSS-g-PANI changed from granular when A-NCP conducted at $t_{C0} - 60$, -50 , or 40 s to columnar at $t_{C0} - 20$ s (Figure 3e–h; Figure S7, Supporting Information). However, the MAPbBr₃ films on PEDOT:PSS had columnar structures regardless of the A-NCP point (Figure 3c,d) because crystallization occurs much faster on PEDOT:PSS than on PSS-g-PANI. As a result, the A-NCP can finely control MAPbBr₃ film morphology on PSS-g-PANI. At a given film thickness, the granular nanograins spatially confine excitons more than the columnar nanograins, so the granular structure has higher EL than columnar structure.

We measured steady-state photoluminescence (PL) and PL lifetime to quantify how the morphology of the MAPbBr₃ film affected its photophysical property. The PL intensities were higher in the MAPbBr₃ film on PSS-g-PANI than in the MAPbBr₃ film on PEDOT:PSS (Figure 4a,b). The PL lifetimes of the MAPbBr₃ films were measured using time-correlated single photon counting (TCSPC). The PL decay curves

(Figure 4c,d) were fitted using the biexponential decay model.^[3] Bare glass/PSS-g-PANI had average PL lifetime $\tau_{avg} = 102.5$ ns, and bare glass/PEDOT:PSS had $\tau_{avg} = 37.1$ ns, demonstrating that the PL lifetimes of MAPbBr₃ films depended on the HILs (Table 1). The differences in PL intensity and lifetime between the MAPbBr₃ films on PEDOT:PSS and PSS-g-PANI were much larger on ITO substrate than on bare glass (Figure 4): ITO/PSS-g-PANI had $\tau_{avg} = 40.33$ ns and ITO/PEDOT:PSS had $\tau_{avg} = 4.736$ ns. We attributed this increased difference to the lower acidity of PSS-g-PANI compared with PEDOT:PSS (Table 2).^[24] The highly acidic PEDOT:PSS etches the ITO; the released In species from the ITO diffuse and cause exciton quenching at the interfaces between PEDOT:PSS and the overlying emitting layer.^[25–27]

Time of flight secondary ion mass spectroscopy (TOF-SIMS) results (Figure 4e) and XPS results (Figure 4f) detected fewer diffused In species on ITO/PSS-g-PANI than on ITO/PEDOT:PSS. We concluded that the highly increased PL intensity and extended PL lifetime of the MAPbBr₃ film on PSS-g-PANI result from increased exciton recombination rate as a consequence of the contributions of the optimized nanograin morphology of the MAPbBr₃ and the reduced amount of diffused In species from the ITO.

The uniform and dense morphology of the MAPbBr₃ film with small grain size provided numerous recombination sites, which limited the diffusion and dissociation of excitons. Strengthened exciton confinement resulting from the granular structure of MAPbBr₃ on PSS-g-PANI also contributed to increasing the exciton recombination rate (Figure 5a).

Finally, we fabricated PeLED devices that had a configuration of ITO/HIL/MAPbBr₃/TPBi/LiF/Al. PSS-g-PANI or PEDOT:PSS were used as the HIL in the devices, and the device characteristics were compared and analyzed. Both PeLEDs had pure green EL centered at 541 nm with FWHM < 20 nm (Figure 5e). The PSS-g-PANI device showed doubled CE and EQE (14.31 cd A⁻¹, 2.96%; luminance: 10 724 cd m⁻²) than the PEDOT:PSS device (7.07 cd A⁻¹, 1.47%; luminance: 6145.4 cd m⁻²) (Figure 5b–d). The PSS-g-PANI device had decreased turn-on voltage (3.59 V for PSS-g-PANI device, 3.88 V for PEDOT:PSS device) defined at the luminance of 1 cd A⁻¹, which was a result of the increased perovskite film quality and better hole-injection. The surface energy level of PSS-g-PANI is formed at a deeper level (5.39 eV) than that of PEDOT:PSS (5.2 eV) and it leads to the enhanced hole-injection to the overlying MAPbBr₃ layer (ionization energy of 6.01 eV).^[3,28] To show the effect of morphology on the device characteristics, we also fabricated and compared PeLED devices that used MAPbBr₃ films on the conducting polymer HILs formed by A-NCP conducted at different dripping time points (Figure S8, Supporting Information). PEDOT:PSS and PSS-g-PANI HIL devices showed the highest CE when the device had uniform MAPbBr₃ films well-packed with small grains. Furthermore, we demonstrated FAPbBr₃ NP LEDs using PSS-g-PANI as HIL (Figure 6). In NP LEDs as well as polycrystalline LEDs, reduced exciton quenching (Figure S9, Supporting Information) and better hole-injection led to the improvement of the device performance, demonstrating significantly high CE and EQE of 37.6 cd A⁻¹ and 7.73% (luminance: 759.4 cd m⁻²) which are higher than those of the PEDOT:PSS-based device (27.7 cd A⁻¹, 5.58%; luminance: 1119 cd m⁻²).

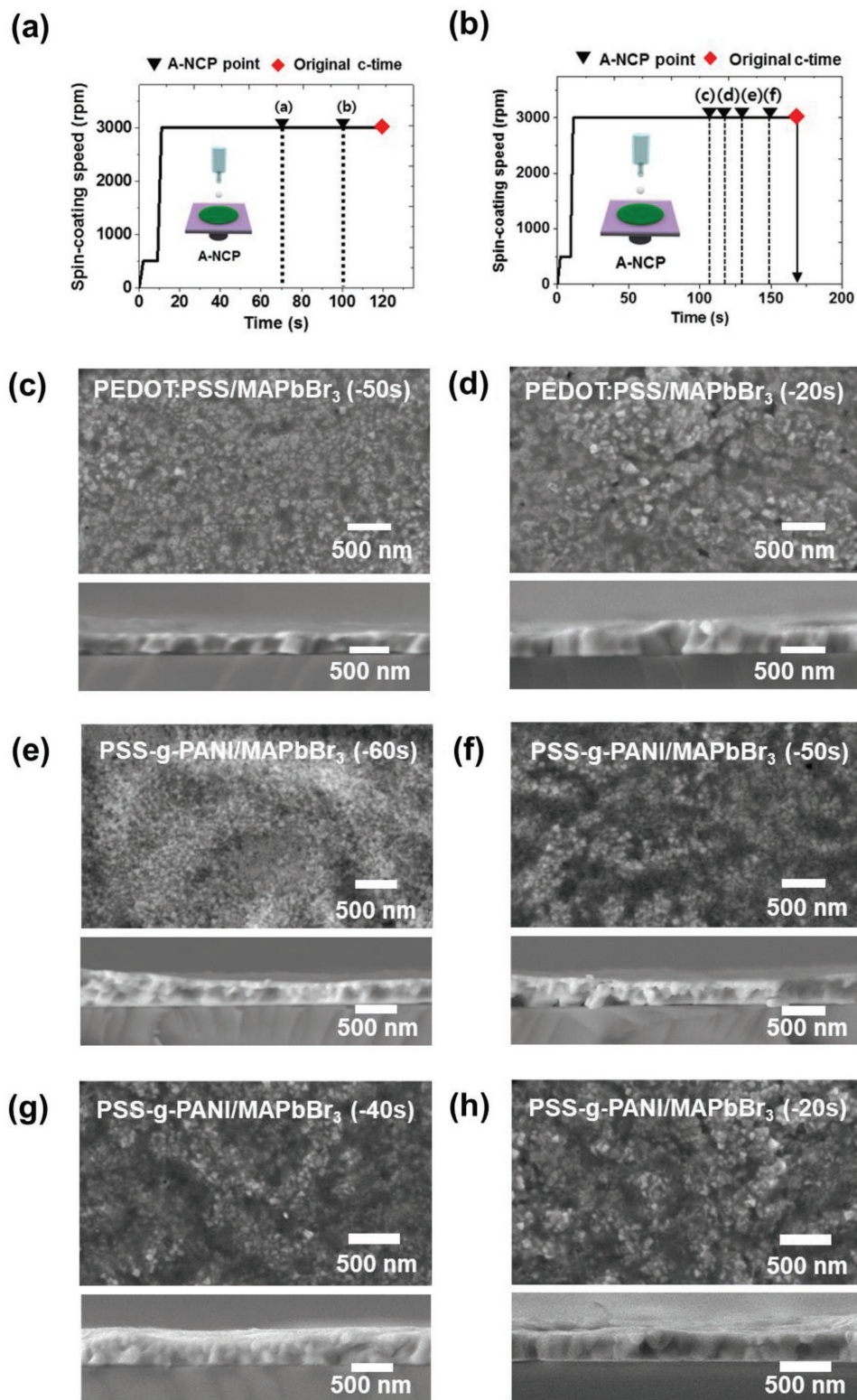


Figure 3. Spin-coating speed-time profile and A-NCP points for the formation of MAPbBr₃ films a) on PEDOT:PSS and b) on PSS-g-PANI. Top-view and cross-sectional SEM images of PEDOT:PSS/MAPbBr₃ and PSS-g-PANI/MAPbBr₃ formed by conducting A-NCP at c) -50 s and d) -20 s from the original crystallization time for PEDOT:PSS/MAPbBr₃ and e) -60 s, f) -50 s, g) -40 s, h) -20 s for PSS-g-PANI/MAPbBr₃.

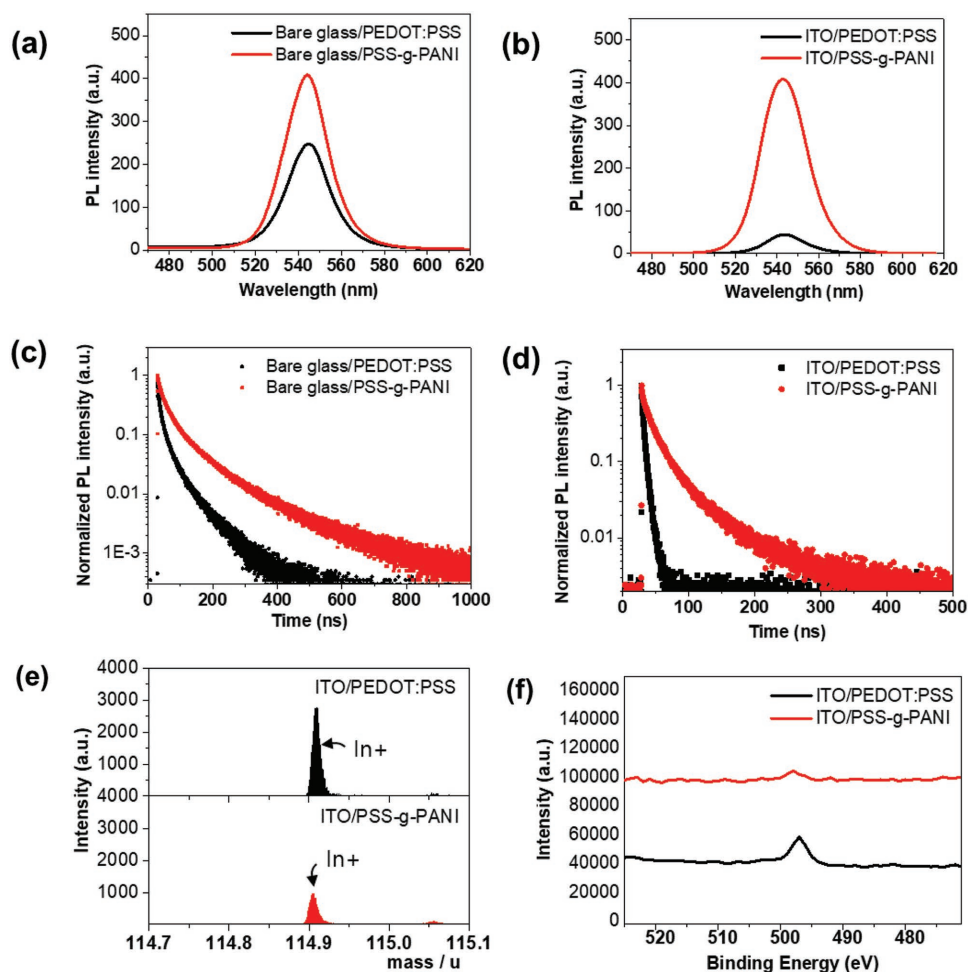


Figure 4. a,b) PL intensity and c,d) PL lifetime of MAPbBr₃ films formed on PEDOT:PSS and PSS-g-PANI when the substrates are a,c) bare glass and b,d) ITO-coated glass. d) TOF-SIMS and f) XPS results of PEDOT:PSS and PSS-g-PANI films on ITO substrates.

3. Conclusion

We introduced an organic-soluble self-doped polyaniline (PSS-g-PANI) as a HIL in polycrystalline PeLEDs. We find that the conducting polymer HIL can effectively control crystallization kinetics of the OHP layer and then we achieved homogeneous small nanogranular perovskite film that increased device efficiency. PSS-g-PANI has high solubility in DMSO which is used as the perovskite precursor solvent; this solubility extended the time required for the full crystallization of the perovskite. Therefore, this significantly retarded crystallization of polycrystalline perovskites using PSS-g-PANI HIL

Table 1. Fast PL lifetime (τ_1), slow PL lifetime (τ_2), and average lifetime (τ_{avg}) of MAPbBr₃ depending on the HIL.

Substrate/HIL	τ_1 [ns]	f_1 [%]	τ_2 [ns]	f_2 [%]	τ_{avg} [ns]
Glass/PEDOT:PSS	12.33	51.05	62.93	48.95	37.10
Glass/PSS-g-PANI	43.11	53.01	169.5	46.99	102.5
ITO/PEDOT:PSS	2.641	46.40	6.551	53.60	4.737
ITO/PSS-g-PANI	18.15	58.37	71.43	41.63	40.33

allows fine control of the A-NCP to make homogeneous granular films with small grains unlike A-NCP on PEDOT:PSS. Therefore, more effective exciton confinement in the granular nanograins can be achieved for more radiative recombination than in columnar structured nanograins that were formed on PEDOT:PSS.

MAPbBr₃ had higher steady-state PL intensity and longer PL lifetime on PSS-g-PANI than on PEDOT:PSS; this difference is evidence that the granular structure increased the exciton recombination rate. Also, the low acidity of PSS-g-PANI, compared with PEDOT:PSS, reduced the number of In species that are released from the ITO electrode due to etching by the acidic polymer solution; this reduction in the In concentration reduced the exciton quenching that occurs at the interface between the HIL and the perovskite layer. Because

Table 2. pH values of a) PEDOT:PSS and b) PSS-g-PANI solutions.

Solution	Acidity [pH]
PEDOT:PSS	2.0
PSS-g-PANI	5.4

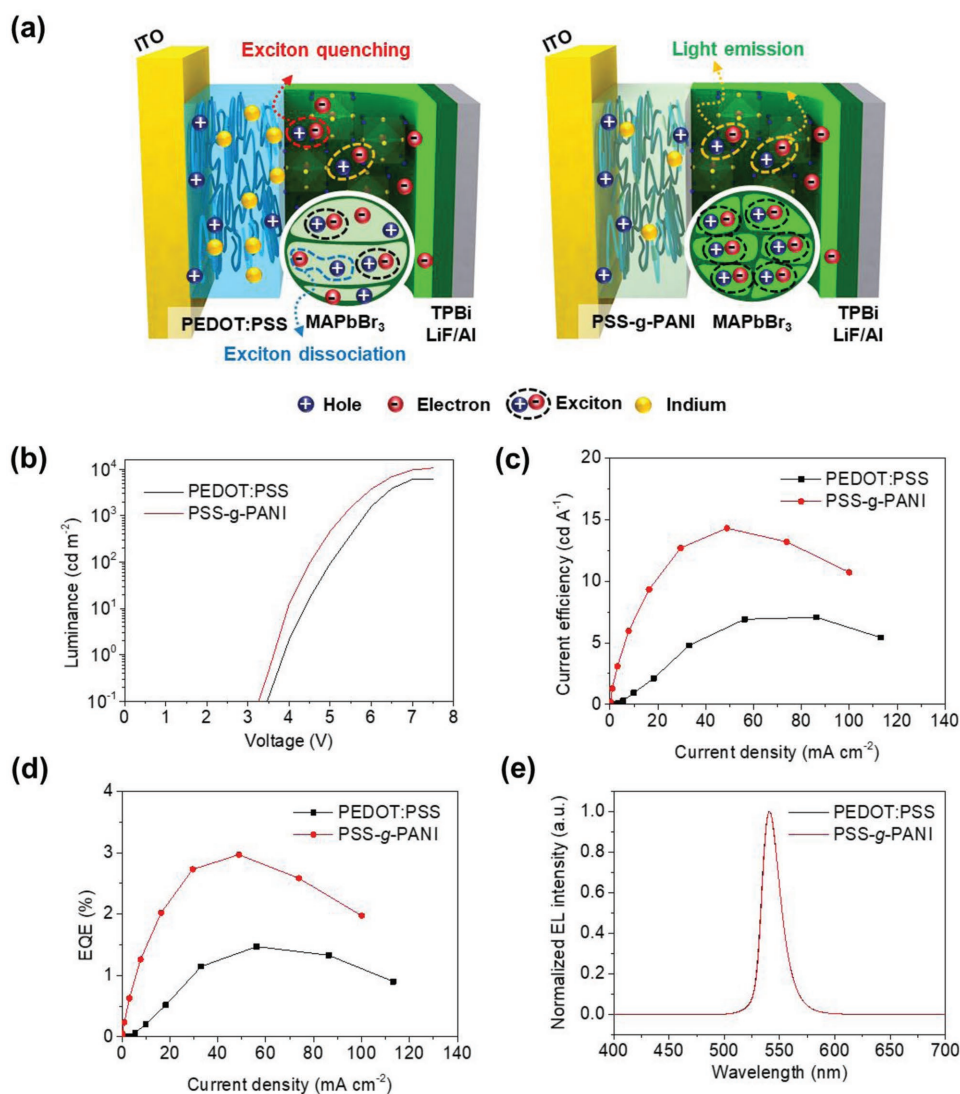


Figure 5. a) Schematic illustrations of exciton quenching by metallic species and exciton dissociation in columnar grains of ITO/PEDOT:PSS-based PeLEDs (left), and efficient light emission from ITO/PSS-g-PANI-based PeLEDs (right). b) Luminance–voltage characteristic. c) Current efficiency–current density characteristic. (d) EQE–current density characteristic. e) EL spectra of ITO/PEDOT:PSS and ITO/PSS-g-PANI PeLEDs.

of the synergetic contributions of optimized perovskite morphology and reduced In diffusion, finally, we achieved high CE of 14.31 cd A⁻¹ in the polycrystalline MAPbBr₃-based PeLEDs using PSS-g-PANI as a HIL, and this value is double that of PeLEDs based on PEDOT:PSS HIL (7.07 cd A⁻¹). Also, PSS-g-PANI demonstrated highly efficient FAPbBr₃ NP LEDs having the CE of 37.6 cd A⁻¹. The findings will contribute to clear understanding the crystallization and luminescence quenching of the OIHPs depending on underlying layers to develop efficient perovskite films for achieving high-efficiency PeLEDs.

4. Experimental Section

Synthesis of PSS-g-PANI: Di-tert-butyl oxo dicarbonate (BOC)₂ (12.5 mmol) and triethylamine (12.5 mmol) were dissolved in a solution of p-aminostyrene (10.0 mmol) in dioxane (50 mL) and then the solution

was stirred for 15 h at 100 °C. Petroleum ether (150 mL) and deionized (DI) water (150 mL) were then added to the solution in sequence. The separation and washing processes were repeated three times to remove impurities. The obtained solution was concentrated and then the BOC-aminostyrene (a white solid) was recrystallized in a yield of 50%. P(SSNa-co-BOC-PMS) was copolymerized with sodium styrenesulfonate (SSNa) and BOC-aminostyrene by using the radical initiator 1,1'-azobis(cyclohexanecarbonitrile) (ACHN). SSNa (24.25 mmol) and BOC-aminostyrene (2.28 mmol) were dissolved in 60 mL DMSO, and then the temperature was increased to 80 °C. ACHN (0.41 mmol) was added dropwise and the solution was stirred for >15 h under N₂ atmosphere. P(SSNa-co-BOC-PMS) was precipitated and filtered with acetone, and the obtained polymer powders were dried in a vacuum at 70 °C for 48 h. Finally, 0.5 g of P(SSNa-co-BOC-PMS) was added to 20 mL of HCl aqueous solution (1 M) and 0.163 mL of aniline was added to the mixture in sequence. The mixture was stirred for 1 h and then chilled at 0 °C, and then 5 mL of ammonium persulfate (134.78 mg) in 1 N HCl aqueous solution was added dropwise, and the solution was stirred for 6 h; the resulting green solution was filtered and purified through a dialysis membrane (Cellu/Sep, MWCO = 2000). Then, PSS-g-PANI with the feeding ratio of PANI to PSS (1:3) was obtained.^[29,30]

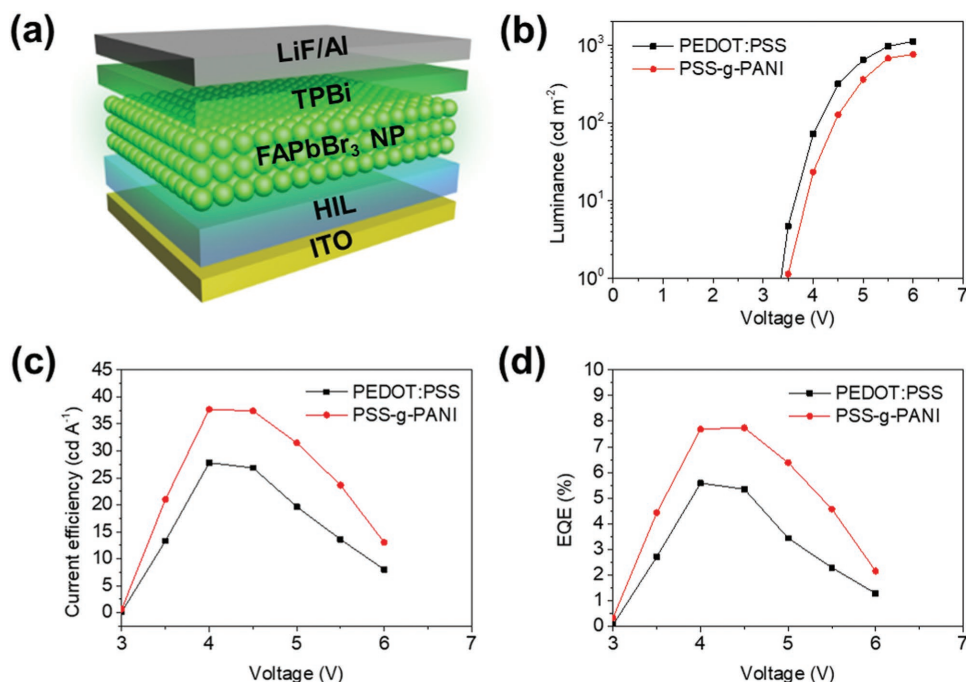


Figure 6. a) Schematic illustration of FAPbBr₃ NP LEDs. b) Luminance–voltage characteristic. c) Current efficiency–voltage characteristic. d) EQE–voltage characteristic of ITO/PEDOT:PSS and ITO/PSS-g-PANI PeNP LEDs.

Perovskite Solution Preparation: To prepare MAPbBr₃ solution (40 wt.%), methylammonium bromide (MABr₃, Dyesol) and lead bromide (PbBr₂, Aldrich) powders were mixed at a molar ratio of MABr:PbBr₂ = 1:1.06, and then dissolved in DMSO (Aldrich) at room temperature while stirring for at least 3 h. FAPbBr₃ NPs were synthesized through ligand-assisted re-precipitation method.^[31]

Measurements: SEM images of Si wafer/HIL/MAPbBr₃ were obtained using a high-resolution field emission SEM (JSM 7401F). The crystal structures of the MAPbBr₃ were defined using an X-ray diffractometer (XRD) (Rigaku, D/MAX-2500). The steady-state photoluminescence (s-s PL) of MAPbBr₃ films was recorded using a spectrofluorometer (JASCO FP6500, Jasco International Co., Ltd., Japan).

The PL lifetimes were determined using TCSPC system. A picosecond pulsed laser with a laser head (LDH-P-C-405, PicoQuant GmbH, Berlin) driven by a PDL 800-B driver (PicoQuant) was used as an excitation source (wavelength: 405 nm, pulse width:<70 ps, repetition rate: 5 MHz). The fluorescence was spectrally filtered by a monochromator (Acton SP-2150i, Princeton Instrument Inc., USA) and the time-resolved fluorescence signal was measured by a TCSPC module (PicoHarp, PicoQuant) combined with a microchannel plate photomultiplier tube (MCP-PMT, R3809U-59, Hamamatsu, Japan).

TOF-SIMS measurement was performed with a TOF-SIMS5 (ION-TF GmbH, Münster, Germany) at the Korea Basic Science Institute (KBSI) Busan Center by using a pulsed 30 KeV Bi⁺ primary beam with a current of 0.29 A. The area used for analysis was a square of 200 × 200 μm. Positive ion spectra were internally calibrated using H⁺, CH₃⁺, C₂H₅⁺, C₃H₇⁺, and C₄H₉⁺ normalized to the respective secondary total ion yields.

AFM images of PEDOT:PSS and PSS-g-PANI films were taken in tapping mode using a Veeco Dimension 3100 unit with Nanoscope V controller. GIXD was measured at beamlines 6D and 9A at the Pohang Accelerator Laboratory (PAL), Korea. An incidence angle of the X-ray beam (λ = 0.1238 Å) was above 0.2°.^[32]

The pH of PEDOT:PSS and PSS-g-PANI solutions were measured using a bench-top pH meter (Thermo Scientific Orion Star A215 pH/conductivity meter).

PeLED Fabrication: Glass substrates with ITO patterns were cleaned by sequential ultrasonic treatment in acetone for 15 min and isopropyl alcohol for 15 min. The cleaned substrates were exposed to UV-ozone

for 20 min to render the surfaces of the substrates hydrophilic. The HILs were formed on the ITO glasses by spin-coating at 3000 rpm for 60 s and baking at 150 °C for 30 min in air. The samples were then moved to a glove box filled with N₂ gas to form MAPbBr₃ films. The prepared MAPbBr₃ solutions were spin-coated and baked at 90 °C for 10 min. MAPbBr₃ nanograin layers were fabricated using A-NCP, which uses dripping of CF:TPBi solution onto the samples during the perovskite spin-coating process. For fabrication of FAPbBr₃ NP LEDs, the prepared FAPbBr₃ solutions were spin-coated at 500 rpm for 7 s and 1000 rpm for 60 s sequentially. Then, 50 nm thick TPBi, 1 nm of lithium fluoride (LiF), and 100 nm of aluminium (Al) were sequentially deposited in a high-vacuum (<10⁻⁷ Torr) thermal evaporator at deposition rates of 1, 0.1, and 3 Å s⁻¹, respectively. The fabricated PeLEDs were encapsulated with a glass lid using UV-epoxy resin under dry N₂ atmosphere.

Supporting Information

Supporting Information is available from the Wiley Online Library or from the author.

Acknowledgements

S.A., M.-H.P., and S.-H.J. contributed equally to this work. This research was supported by the Nano Material Technology Development Program through the National Research Foundation of Korea (NRF) funded by the Ministry of Science and ICT (NRF-2014M3A7B4051747) and by the National Research Foundation of Korea (NRF) grant funded by the Korea government (Ministry of Science and ICT) (NRF-2016R1A3B1908431). Also, this research was supported by Creative Materials Discovery Program through the National Research Foundation of Korea (NRF) funded by Ministry of Science and ICT (2018M3D1A1058536).

Conflict of Interest

The authors declare no conflict of interest.

Keywords

crystal structure, exciton confinement, exciton quenching, hole injection material, perovskite light-emitting diode

Received: October 25, 2018

Revised: November 26, 2018

Published online: December 18, 2018

- [1] Z.-K. Tan, R. S. Moghaddam, M. L. Lai, P. Docampo, R. Higler, F. Deschler, M. Price, A. Sadhanala, L. M. Pazos, D. Credgington, F. Hanusch, T. Bein, H. J. Snaith, R. H. Friend, *Nat. Nanotechnol.* **2014**, *9*, 687.
- [2] Y.-H. Kim, H. Cho, J. H. Heo, T.-S. S. Kim, N. Myoung, C.-L. Lee, S. H. Im, T.-W. Lee, *Adv. Mater.* **2015**, *27*, 1248.
- [3] H. Cho, S.-H. Jeong, M.-H. Park, Y.-H. Kim, C. Wolf, C.-L. Lee, J. H. Heo, A. Sadhanala, N. Myoung, S. Yoo, S. H. Im, R. H. Friend, T.-W. Lee, *Science* **2015**, *350*, 1222.
- [4] N. K. Kumawat, A. Dey, K. L. Narasimhan, D. Kabra, *ACS Photonics* **2015**, *2*, 349.
- [5] G. Li, Z. K. Tan, D. Di, M. L. Lai, L. Jiang, J. H. W. Lim, R. H. Friend, N. C. Greenham, *Nano Lett.* **2015**, *15*, 2640.
- [6] Z. Xiao, R. A. Kerner, L. Zhao, N. L. Tran, K. M. Lee, T.-W. Koh, G. D. Scholes, B. P. Rand, *Nat. Photonics* **2017**, *11*, 108.
- [7] M. H. Park, S. H. Jeong, H. K. Seo, C. Wolf, Y. H. Kim, H. Kim, J. Byun, J. S. Kim, H. Cho, T. W. Lee, *Nano Energy* **2017**, *42*, 157.
- [8] S.-H. Jeong, S.-H. Woo, T.-H. Han, M.-H. Park, H. Cho, Y.-H. Kim, H. Cho, H. Kim, S. Yoo, T.-W. Lee, *NPG Asia Mater.* **2017**, *9*, e411.
- [9] X. Yang, X. Zhang, J. Deng, Z. Chu, Q. Jiang, J. Meng, P. Wang, L. Zhang, Z. Yin, J. You, *Nat. Commun.* **2018**, *9*, 2.
- [10] G. E. Eperon, V. M. Burlakov, P. Docampo, A. Goriely, H. J. Snaith, *Adv. Funct. Mater.* **2014**, *24*, 151.
- [11] J. C. Yu, D. Bin Kim, E. D. Jung, B. R. Lee, M. H. Song, *Nanoscale* **2016**, *8*, 7036.
- [12] G. Han, T. M. Koh, S. S. Lim, T. W. Goh, X. Guo, S. W. Leow, R. Begum, T. C. Sum, N. Mathews, S. Mhaisalkar, *ACS Appl. Mater. Interfaces* **2017**, *9*, 21292.
- [13] S. Kumar, J. Jagielski, S. Yakunin, P. Rice, Y.-C. Chiu, M. Wang, G. Nedelcu, Y. Kim, S. Lin, E. J. G. Santos, M. V. Kovalenko, C.-J. Shih, *ACS Nano* **2016**, *10*, 9720.
- [14] H. Yin, L. Jin, Y. Qian, X. Li, Y. Wu, M. S. Bowen, D. Kaan, C. He, D. I. Wozniak, B. Xu, A. J. Lewis, W. Shen, K. Chen, G. E. Dobreiner, Y. Zhao, B. B. Wayland, Y. Rao, *ACS Appl. Energy Mater.* **2018**, *1*, 1476.
- [15] N. F. Jamaludin, N. Yantara, Y. F. Ng, M. Li, T. W. Goh, K. Thirumal, T. C. Sum, N. Mathews, C. Soci, S. Mhaisalkar, *ChemPhysChem* **2018**, *19*, 1075.
- [16] C. A. Cutler, M. Bouguettaya, T. S. Kang, J. R. Reynolds, *Macromolecules* **2005**, *38*, 3068.
- [17] A. Cho, S. Kim, S. Kim, W. Cho, C. Park, F. S. Kim, J. H. Kim, *J. Polym. Sci., Part B: Polym. Phys.* **2016**, *54*, 1530.
- [18] H. Kim, S. Nam, H. Lee, S. Woo, C. S. Ha, M. Ree, Y. Kim, *J. Phys. Chem. C* **2011**, *115*, 13502.
- [19] H.-K. Seo, H. Kim, J. Lee, M.-H. Park, S.-H. Jeong, Y.-H. Kim, S.-J. Kwon, T.-H. Han, S. Yoo, T.-W. Lee, *Adv. Mater.* **2017**, *29*, 1605587.
- [20] A. Kojima, K. Teshima, Y. Shirai, T. Miyasaka, *J. Am. Chem. Soc.* **2009**, *131*, 6050.
- [21] B. Ding, Y. Li, S. Y. Huang, Q. Q. Chu, C. X. Li, C. J. Li, G. J. Yang, *J. Mater. Chem. A* **2017**, *5*, 6840.
- [22] A. A. Zhumekenov, V. M. Burlakov, M. I. Saidaminov, A. Alofi, M. A. Haque, B. Turedi, B. Davaasuren, I. Dursun, N. Cho, A. M. El-Zohry, M. De Bastiani, A. Giugni, B. Torre, E. Di Fabrizio, O. F. Mohammed, A. Rothenberger, T. Wu, A. Goriely, O. M. Bakr, *ACS Energy Lett.* **2017**, *2*, 1782.
- [23] V. K. Lamer, R. H. Dinegar, *J. Am. Chem. Soc.* **1950**, *72*, 4847.
- [24] J. W. Jung, J. U. Lee, W. H. Jo, *J. Phys. Chem. C* **2010**, *114*, 633.
- [25] T.-W. Lee, Y. Chung, O. Kwon, J.-J. Park, *Adv. Funct. Mater.* **2007**, *17*, 390.
- [26] M. P. de Jong, L. J. van IJzendoorn, M. J. A. de Voigt, *Appl. Phys. Lett.* **2000**, *77*, 2255.
- [27] Y. Meng, Z. Hu, N. Ai, Z. Jiang, J. Wang, J. Peng, Y. Cao, *ACS Appl. Mater. Interfaces* **2014**, *6*, 5122.
- [28] K.-G. Lim, S. Ahn, H. Kim, M.-R. Choi, D. H. Huh, T.-W. Lee, *Adv. Mater. Interfaces* **2016**, *3*, 1500678.
- [29] W. J. Bae, K. H. Kim, Y. H. Park, W. H. Jo, *Chem. Commun.* **2003**, 2768.
- [30] M.-R. Choi, T.-H. H. Han, K.-G. Lim, S.-H. Woo, D. H. Huh, T.-W. Lee, *Angew. Chem., Int. Ed.* **2011**, *50*, 6274.
- [31] X. Y. Chin, A. Perumal, A. Bruno, N. Yantara, S. A. Veldhuis, L. Martinez-Sarti, B. Chandran, V. Chirvony, A. S.-Z. Lo, J. So, C. Soci, M. Gratzel, H. J. Bolink, N. Mathews, S. G. Mhaisalkar, *Energy Environ. Sci.* **2018**, *11*, 1770.
- [32] M. Jang, S. H. Kim, H. K. Lee, Y. H. Kim, H. Yang, *Adv. Funct. Mater.* **2015**, *25*, 3833.